Fractographic analysis of austempered ductile iron

D. O. FERNANDINO and R. E. BOERI

Metallurgy Division, INTEMA – National University of Mar del Plata – CONICET, Mar del Plata B7608FDQ, Argentina

ABSTRACT This investigation involves a systematic study of the fracture surfaces of two grades of austempered ductile iron (ADI) broken under quasi-static, dynamic and cyclic loading conditions. The study used electron microscopy, optical microscopy and image post-processing. The results show that the predominating fracture mechanism in ADI upon impact loading changes from quasi-cleavage to ductile (with little areas of cleavage facets) as the testing temperature increases. Noticeably, even at the lower temperatures tested, the fracture surface of ADI shows clear signs of ductile fracture mechanisms. In particular, graphite nodule cavities suffer marked plastic deformation. Fracture after bending tests at room temperature was characterized by a mix of quasi-cleavage facets, deformation of the contour of nodular cavities and microvoid coalescence. In the case of fatigue fracture at room temperature, the fracture surfaces show a flat appearance which has notorious differences with those reported for other loading conditions, but the typical fatigue striations were not found. The particular features identified on the fatigue fracture surfaces can be used to identify fatigue failures.

It was also shown that the determination of the direction of main crack propagation by using the experimental methodology proposed earlier by the authors is applicable to ADI fractured by impact and quasi-static loads.

The results provide information potentially useful to fractographic analyses of ADI, particularly in samples that fail in service under unknown conditions.

Keywords austempered ductile iron; bending; fatigue; fractography; fracture surface; impact.

NOMENCLATURE
L' = Projected length of the fracture profile
Lt = Fracture profile length
Rs = Superficial roughness
Ry = Peak to valley ratio from the fracture profile
Y = Length of the nodular contour in parallel axis to the main crack propagation direction
X = Length of the nodular contour in perpendicular axis to the main crack propagation direction
B = Angle between the major axis of the equivalent ellipse and the main crack propagation direction

INTRODUCTION

The austempered ductile iron (ADI) is a member of the ductile iron (DI) family which is produced by means of an austempering heat treatment. The different grades are produced primarily by varying the austempering temperature and duration of the heat treatment cycle.[1] Nearly twice as strong as pearlitic DI, ADI still retains high elongation and toughness. This combination provides a material with superior tensile strength, wear resistance and fatigue strength. Its usual applications include gears, crankshafts, connecting rods, agricultural and construction ground engaging parts such as plow points, digger teeth and track shoes, shafts; cams; mining and grinding equipment such as balls and hammers; mill liners and rollers; spring hanger brackets and railroad wear applications. Because of its outstanding mechanical properties, ADI represents an excellent choice of replacement for

Correspondence: D. O. Fernandino. E-mail: dfernandino@fi.mdp.edu.ar

hardened and tempered forged and cast steel.[2] However, in spite of its increasing application, when the fracture process of ADI and more specifically the dominating failure mode of parts that failed in service are analysed, a lack of knowledge is evident. In general, the graphite nodules present in the microstructure, which act as stress concentrators, lead to fracture surfaces of complex characteristics. The non-metallic nature of the graphite nodule that is inserted in the metallic matrix notoriously affects the appearance of the fracture surface.[3,4] Most of the fractographic studies focused on ADI are secondary parts of analyses of mechanical properties.[5–7] Few papers focus on the fractography of DI.[8–13] In this context, this lack of knowledge may become a limiting factor for the failure analysis of ADI.

The goal of this work is to characterize the influence of different loading conditions on the morphology of the fracture surfaces of ADI. The study involves two strength grades of ADI and focuses on the characterization of the topographic features of the fracture surfaces and their relation with the dominant failure mode. In addition, the study aims at identifying the main crack propagation direction by means of experimental methodologies proposed by the authors in a recent paper.[12,13]

EXPERIMENTAL PROCEDURE

The material used in this study was obtained from one-inch 'Y' blocks of DI. The chemical composition was determined by using a Baird DV6 spectrometer. 'Y' blocks were ferritized in order to improve the machinability and to standardize the initial microstructure before the austempering heat treatment to obtain ADI is carried out. This procedure is reported as a method to attain better control of the microstructure at the austenitizing temperature.[1] Ferritizing consisted of an austenitizing stage at 920 °C for 4 h followed by a slow cooling stage down to room temperature. In addition, two conventional austempering heat treatment cycles consisting of an austenitizing stage at 900 °C for 1 h followed by isothermal heat treatments at 360 °C and 280 °C for 90 min were made in order to obtain two different grades of ADI. Metallographic samples were prepared by standard cutting, grinding and polishing methods, and were etched using nital (2%). The microconstituents were quantified by using an optical microscope OLYMPUS PMG3 and the Image Pro Plus software. V-notched Charpy impact specimens of $10 \times 10 \times 55$ mm and SEN (B) specimens were machined from the calibrated zones of 'Y' blocks according to ASTM E23 standard.

Brinell hardness measurements were performed using a universal hardness testing machine IBERTEST, Model 'DU-250' following ASTM E10-01. All reported values

of mechanical properties are the average of at least three tests. Three point bending tests with quasi static (Bending), dynamic (Impact) and cyclic (Fatigue) loading condition were performed. Impact testing was carried out by using a pendulum AMSLER 130/688, with a maximum energy of 300 J. Bending tests were performed using a universal testing machine Morh&Federhaff with a cross-head displacement rate of 8.4×10^{-3} mm/s. A high cycle fatigue regime test was performed in a displacement controlled mechanical testing machine with a double eccentric actuator. A maximum load of 2 kN was induced by means of a constant eccentricity of e = 0.145 mm.[14] A stress ratio R = 0 was chosen for all tests. Stable crack propagation was attained following these conditions under small-scale plasticity. The frequency of the cyclic load was of 25 Hz.

The fracture surfaces of the broken specimens were observed by means of a scanning electron microscopy (SEM) and the fracture profiles revealed by optical microscopy. Following the methodology reported in a recent paper by the authors[13], the fracture profiles were quantitatively characterized by means of surface roughness parameters. The numerical quantification was carried out by using the Image-Pro Plus software, and the results were the average of at least 20 fields in five successive levels. The methodology involves the use of a stereology equation[15] in order to determine the magnitude of the actual fracture surface considering its roughness (Rs) as follow:

$$Rl(mm/mm) = \left(\frac{Lt}{L'}\right) \tag{1}$$

$$Rs = \left(\frac{4}{\pi}\right)(Rl - 1) + 1 = \left(\frac{St}{SA}\right) \tag{2}$$

$$Ry\ (mm/mm)\ =\ (Y_{max}/Y_{min}) \tag{3}$$

where the Lt value is the measurement of the actual length of the fracture profile, whereas the L' value is the projected length of the fracture profile. From the measurement of Lt and L' on the fracture profiles, Rl and Rs values were calculated, in each case, using Eqs. (1) and (2), respectively. Rs give a measure of the surface roughness. Additionally, the height of the highest peak (Y_{max}) and the height of the deepest valley (Y_{min}) of the fracture profile are measured, and the Ry values were calculated from Eq. (3). A schematic representation is shown in Fig. 1
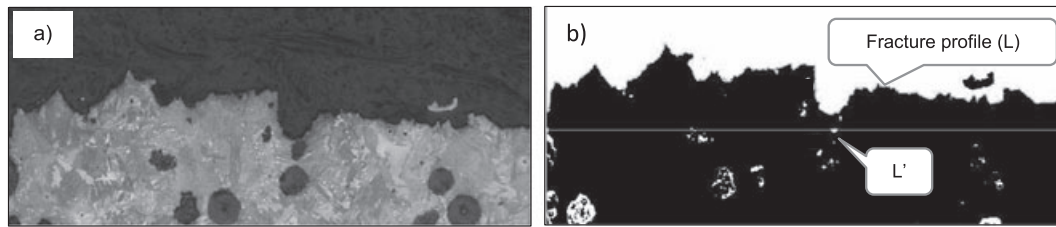
Fig. 1 Schematic representation of the roughness parameter used, following the methodology reported by Fernandino *et al.* (2015). Fracture profile resulting of Impact test at −20 °C on ADI_{360} (100×). a) Optical micrograph; b) quantification of digitalized image using Image-Pro Plus software.

RESULTS AND DISCUSSION

Chemical composition and microstructures

The chemical composition of the DI used is listed on Table 1. The composition is slightly hypoeutectic and includes small amounts of Cu and Mn, needed to confer sufficient austemperability to obtain a fully ausferritic matrix along the entire sample volume after the austempering heat treatment. The characterization of the as-cast microstructure is listed in Table 2. High nodularity and a reasonable nodule count were obtained; consequently, the melt is considered suitable for this study.

The microstructures resulting from as cast condition and after the austempering heat treatment cycles are shown in Fig. 2. The mechanical properties of each microstructure are listed in Table 3. According to ASTM A897M-03, ADI grades 150-110-07 (ADI_{360}) and 200-75-02 (ADI_{280}) are obtained. The results are in concordance with the data reported in specific literature for this kind of DI.[1]

Characterization of the fracture surfaces
Impact

The fracture surfaces resulting from impact loading on ADI_{360} and ADI_{280} samples are shown in Figs. 3 and 4 respectively. As a general feature, graphite nodules and nodular cavities free from graphite nodules were observed at all temperatures. At −20 °C (see Fig. 3a), the fracture surfaces show a dominating brittle failure mode consisting of quasi-cleavage facets and some areas of plastic deformation (dimples) mainly located on the contour of the nodular cavities and at planes joining different cleavage facets. An important characteristic that must be noted is that all graphite nodule cavities have expanded,

and the nodules appear to be separated from the matrix. This has been so even for the harder ADI_{280} grade (Fig. 4a). It is also important to note that for these grades of ADI, the lower and upper shelf temperatures are approximately located at −120 °C and 60 °C respectively.[9,16] Consequently, a temperature of −20 °C is located within the ductile to brittle transition temperature range. This could justify the observation of brittle and ductile fracture mechanisms simultaneously; however, the characteristic failure mode reported at lower shelf temperatures is also quasi-cleavage. As the test temperature increases, a greater deformation of the nodular contour is observed. In addition, larger areas of extensive plastic deformation of the metallic matrix are found. At 60 °C (see Figs. 3d & 4d), growth of the nodular cavities, inclusions and eventually nucleated microvoids became more notorious. This is shown in better detail in Fig. 5. This has been the case for both ADI grades investigated.

The characteristic features typically found in the fracture surface of ADI when the dominating failure mode is brittle are shown in Fig. 5a. The quasi-cleavage facets observed for ADI are smaller than those found for both ferritic and pearlitic DI.[12,13] Adjacent cleavage facets show notorious tearing between them. This ductile feature was not found neither on ferritic nor on pearlitic DI.[12,13] These differences justify the higher toughness of ADI in comparison with DI of other microstructures. The higher toughness can be explained by the quasi-cleavage fracture process itself, where the fracture initiates along the cleavage facets and follows by plastic strain of the remaining ligament. Meanwhile in the cleavage mechanism the fracture process is characterized by the separation of the cleavage planes through its edges.[17] In pearlitic DI, the crack propagates along the cleavage plane of the ferrite through pearlite colonies. However,
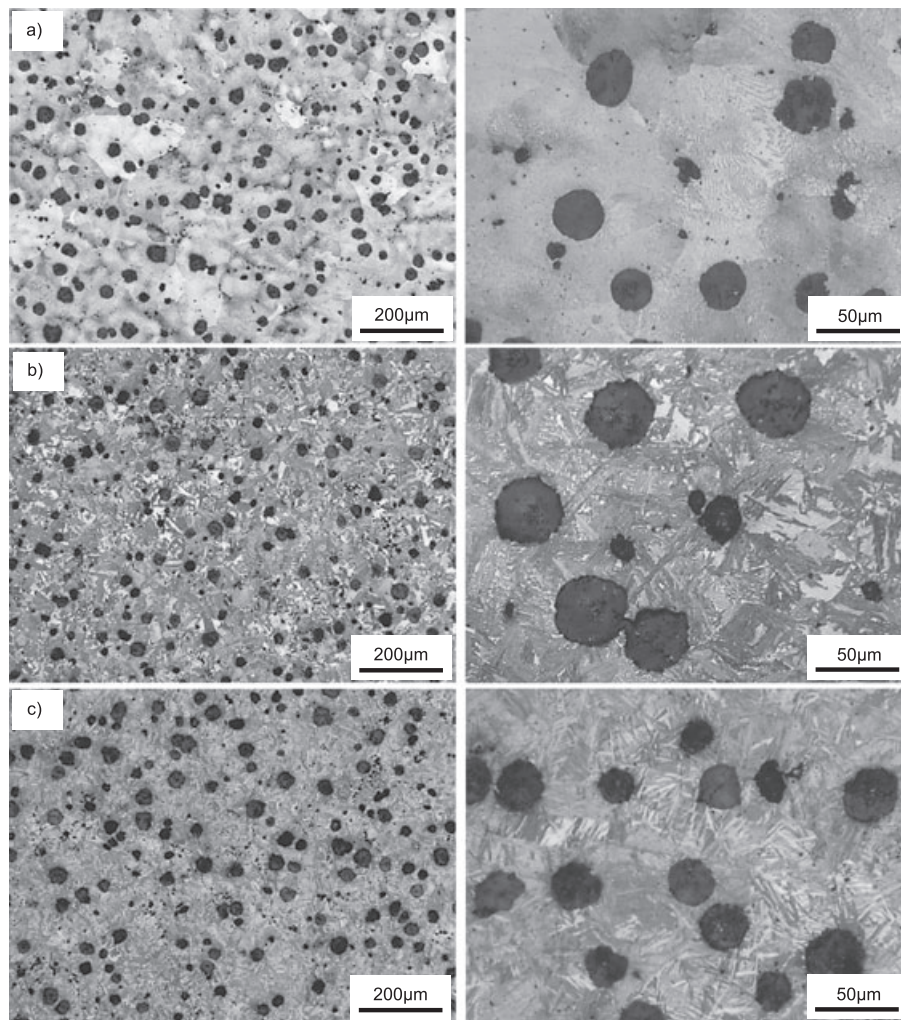
Table 1 Chemical composition (wt%)

C	Si	Mn	S	P	Mg	Cu	Ni	Cr
3.32	2.36	0.31	0.012	0.016	0.033	0.62	0.025	0.058

Table 2 Characterization of as-cast microstructure

Metallic matrix	Nodularity	Nodule size	Nodule count [nods/mm^2]
Pearlitic	>95%	6	100

Fatigue Fract Engng Mater Struct, 2016, **39**, 583–598

Fig. 2 Optical micrographs at magnifications of 100× and 200× respectively. a) Pearlitic (As-Cast); b) austempered at 360 °C (ADI$_{360}$); c) austempered at 280 °C (ADI$_{280}$).

Table 3 Mechanical properties of each microstructure

Microstructure	Mechanical properties			
	Brinell hardness	0.2% yield strength [MPa]	Ultimate tensile strength [MPa]	Elongation [%]
Pearlitic	272	480	720	5
ADI360	350	825	1050	11
ADI 280	456	1150	1577	4

in ADI, a different fracture surface topology with smaller quasi-cleavage facets is observed. This morphological change of the fracture surfaces are associated with the dimensions of the ausferritic laths, remarking the importance of the microstructure in the fracture, particularly when brittle fracture is the dominating fracture mode.

The smaller size of the cleavage facets was associated with the tendency of the crack to propagate through the metallic matrix along the ferrite–austenite interface, which characteristic dimensions are smaller than the lamellas of pearlite and ferrite grains.[18,19]

Figure 5b and c shows the characteristics of the ductile failure mode. Noticeable plastic deformation of the nodular cavities, small amounts of quasi-cleavage areas and extensive microvoid formation are shown.

In summary, under impact loads, the predominant failure mode of ADI changes from predominant quasi-cleavage at the lower temperature, to ductile, with a small amount of isolated quasi-cleavage facets at the higher test temperature.

Profiles of fracture surfaces resulting of impact tests of ADI$_{360}$ at -20 °C and 60 °C were examined by optical micrography on samples mounted in bakelite. The resulting roughness values are shown in Fig. 6a and b
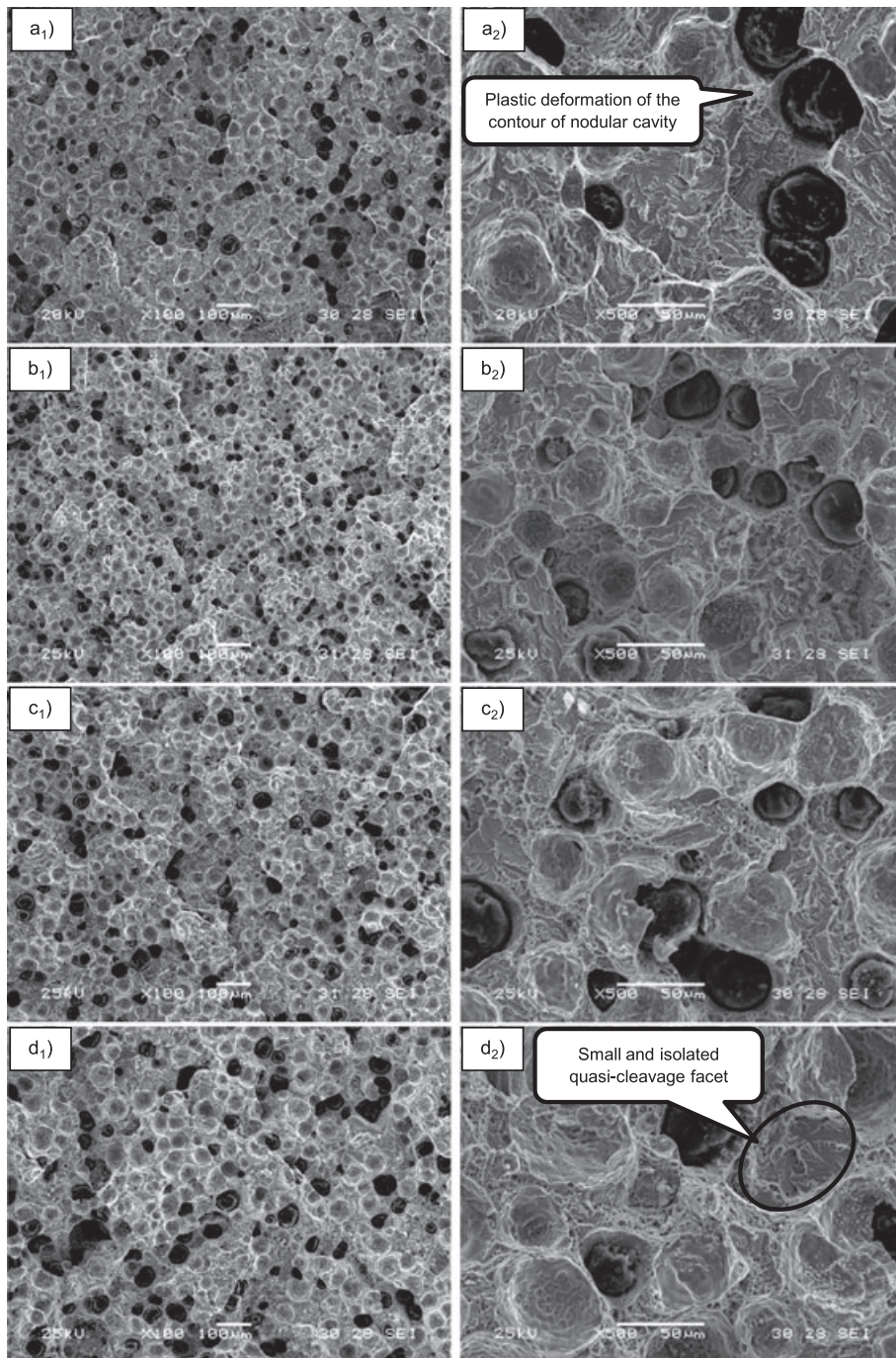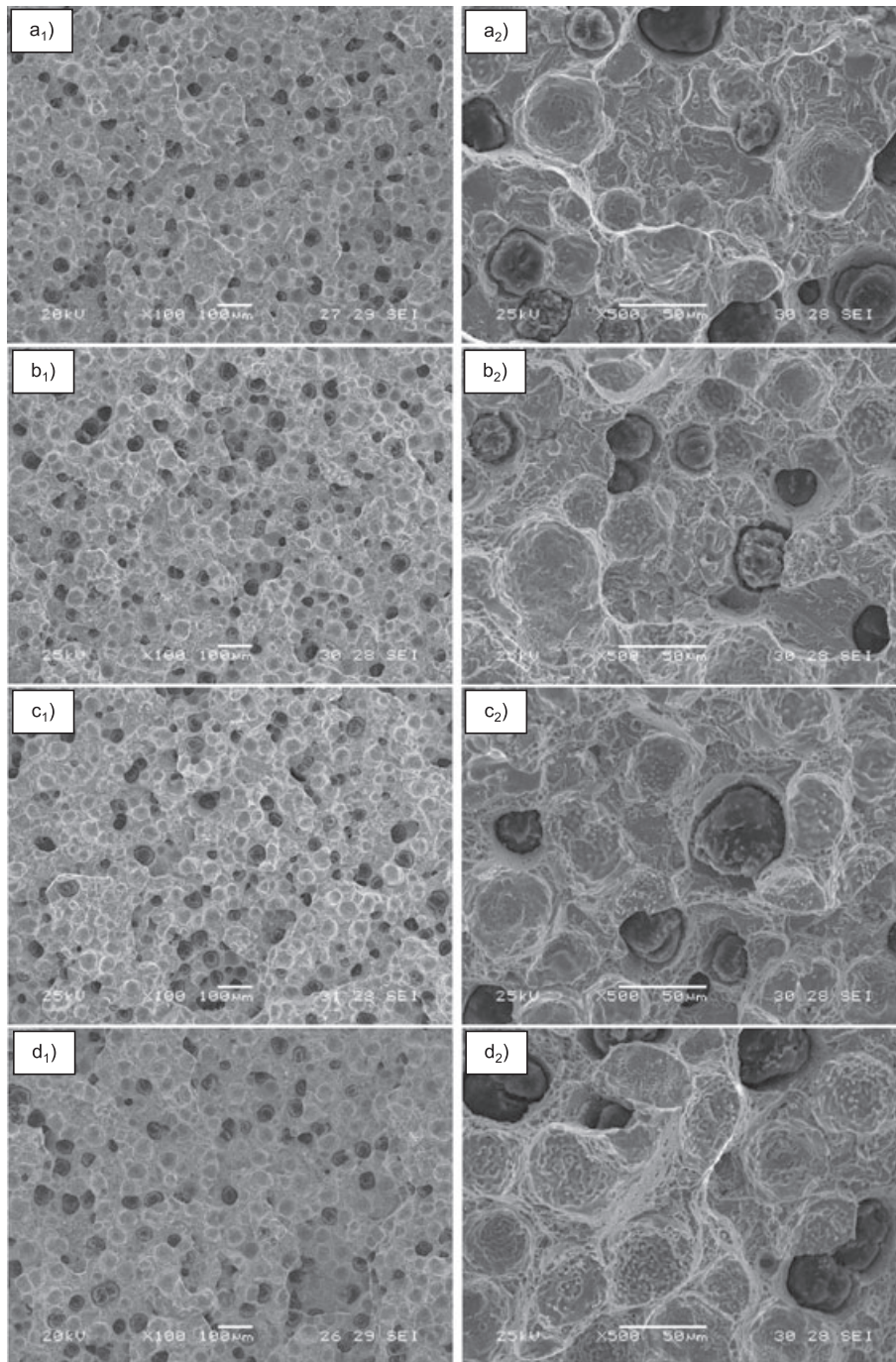
Fig. 3 SEM image of the fracture surface resulting of impact tests at different temperature on ADI_{360}. a) $-20\,°C$; b) $0\,°C$; c) $20\,°C$; d) $60\,°C$.

respectively. Note that both Rs and Ry values increase by approximately 10% and 18% respectively as the test temperature increases. Similar results are obtained for ADI_{280} samples, where the increase in Rs and Ry reaches 7% and 21% respectively. These results are in concordance with the SEM images and allow concluding that the crack propagation path follows more tortuous patterns as the temperature increases.

Bending

The fracture surfaces resulting from three point bending tests under quasi-static loading conditions at room temperature are shown in Figs. 7 and 8 for both ADI grades tested. As reported above for impact tests, the fracture surface is characterized by plastic deformation of the contours of nodular cavities and portions of the matrix,
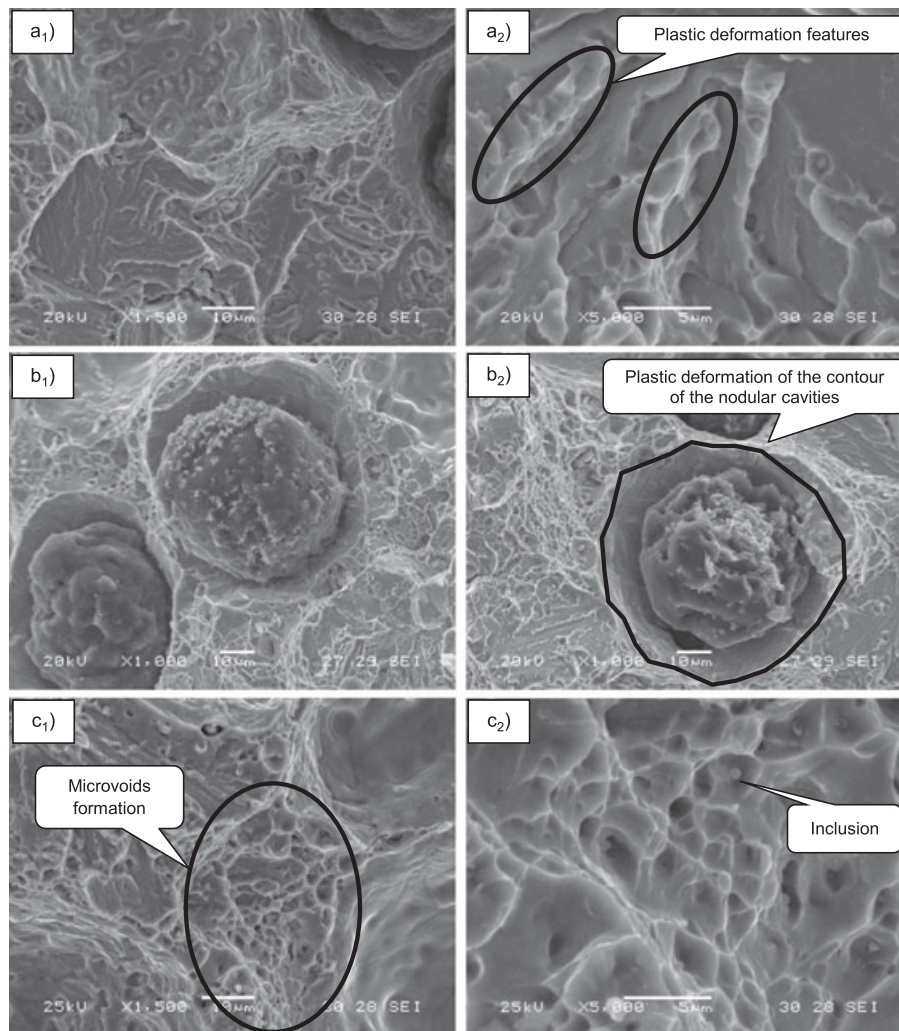
Fig. 4 SEM image of the fracture surface resulting of impact tests at different temperature on ADI_{280}. a) $-20\,°C$; b) $0\,°C$; c) $20\,°C$; d) $60\,°C$.

mixed with isolated quasi-cleavage facets (marked by white arrows), as shown in Fig. 7a and b. Figure 7c shows a detail of a quasi-cleavage zone marked by a dotted square in Fig. 7b. Extensive plastic deformation is found, as revealed by the noticeable formation of microvoids, Fig. 7d. Similar results were found ADI_{280} samples (see Fig. 8). These results are similar to those reported by

other authors after the analysis of the fracture surfaces resulting of tensile tests samples.[10,20]

The optical micrographs of fracture profiles resulting from bending tests at room temperature and the corresponding roughness values are shown in Fig. 9. Both, Rs and Ry values are between approximately 20% and 10% greater than those measured on samples

Fig. 5 SEM image of the fracture surface resulting of impact tests at different temperature on ADI_{360}. a) Detail of a quasi-cleavage facet at $-20\,°C$; b) plastic deformation of nodular cavities at $60\,°C$; c) plastic deformation along the ausferritic matrix at $60\,°C$.

broken by impact testing at $-20\,°C$ and $60\,°C$ respectively. Similar results were obtained for ADI_{280}. These results show that the quasi-static loading condition promotes fracture surfaces of greater roughness, mainly as a result of a greater plastic deformation along the metallic matrix and the contour of the nodular cavities.

Fatigue

The fracture surface resulting from three point bending tests with cyclic loading conditions at room temperature of ADI_{360} after 1.6×10^5 fatigue cycles is shown in Fig. 10. It is possible to identify a change in the fracture surface topology related to differences between the fatigue crack propagation zone (A) and the final fracture region (B).

Figures 11 and 12 show the fracture surfaces after fatigue testing for ADI_{360} and ADI_{280} respectively. At low magnification the surface of the fatigue grown crack shows graphite nodules and nodular cavities free from graphite nodules exposed and an apparently flat fracture surface topology (see Figs. 11a & 12a). As the magnification is increased (see Fig. 9b), the surface shows some secondary cracks (marked by white arrows). Different from the observations for impact and bending, in this case, the contours of the graphite nodule cavities show very little plastic deformation. The fatigue crack propagation along the matrix, Figs. 11c and d and 12c and d, does not follow the striation mechanism, but is characterized by a cleavage-like fracture surface. Both, the lack of striations and the cleavage-like mechanism of fatigue fracture advance are commonly described in the literature for high strength metallic alloys.[21–25] Some authors
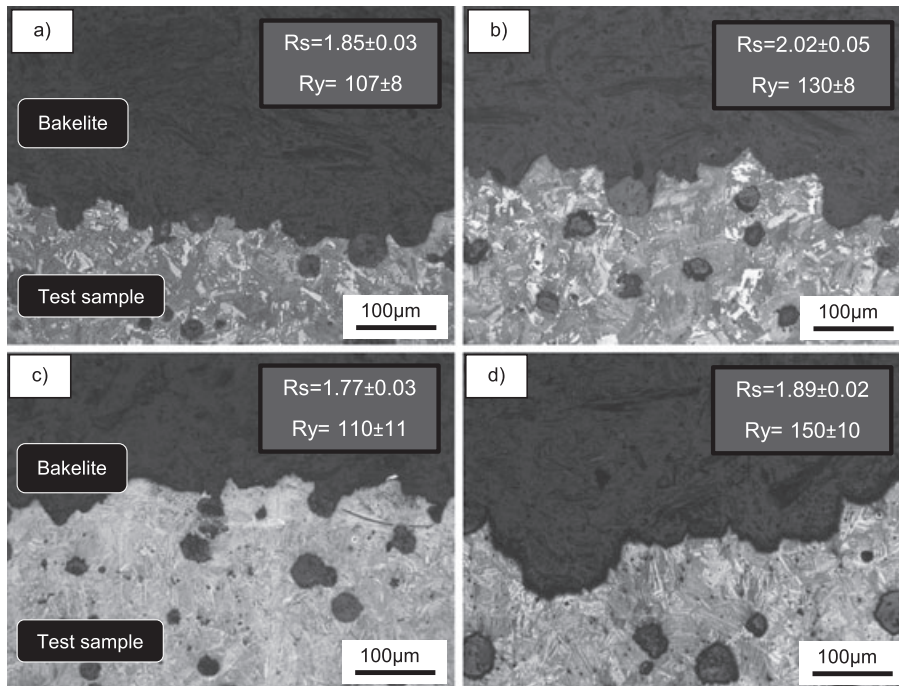
Fig. 6 Optical micrographs of the fracture profile resulting of impact test at (100×). a) ADI360 −20 °C; b) ADI_{360} 60 °C; c)ADI_{280} −20 °C; b) ADI_{280} 60 °C.
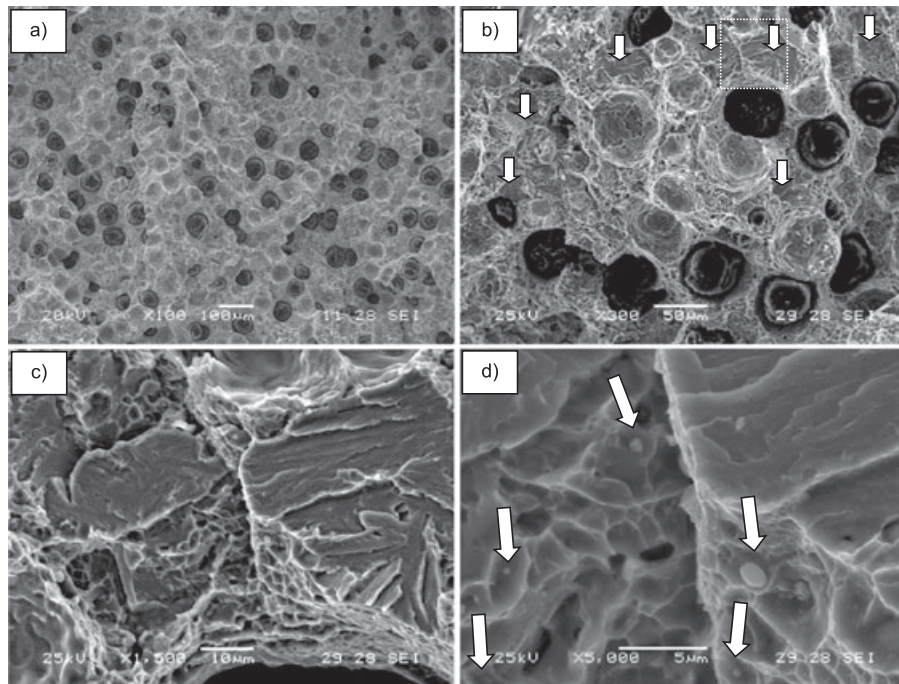
Fig. 7 SEM image of the fracture surface resulting from bending tests at room temperature on ADI_{360}. Different magnifications.

proposed that, at high growth rates, crack propagation rates become sensitive to microstructure and load ratio, consistent with the occurrence of 'static' fracture modes during striation growth (e.g. intergranular and cleavage cracking).[21,22] On the contrary, it is also reported that cleavage-like faceted appearance dominates in many materials at very low ΔK levels.[24] However, similar fractographic characteristics have been reported by other authors for ADI tested under different fatigue conditions, such as different applied loads, stress ratios
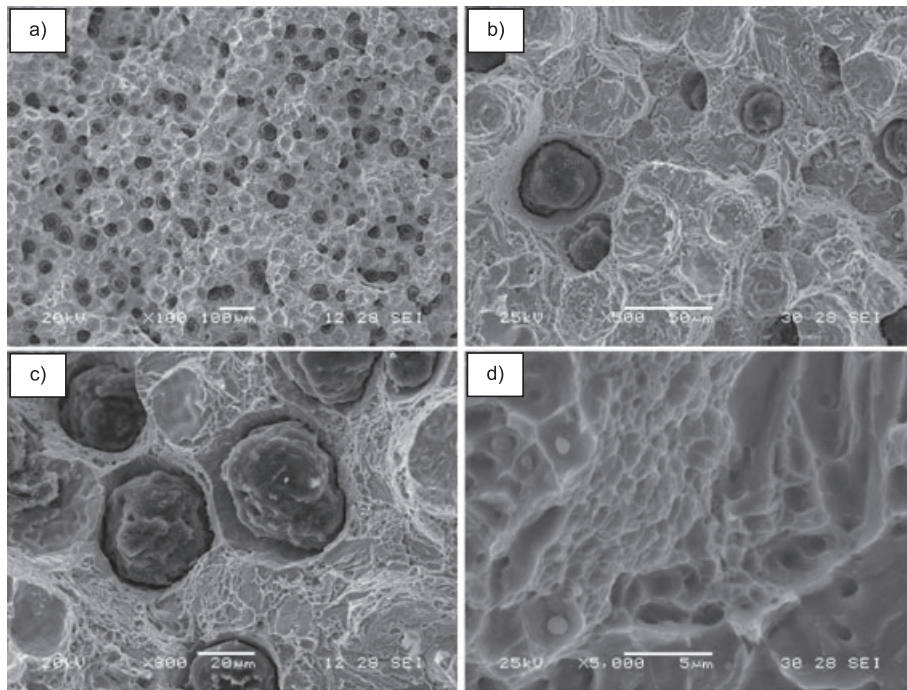
Fig. 8 SEM image of the fracture surface resulting from bending tests at room temperature on ADI_{360}. Different magnifications.
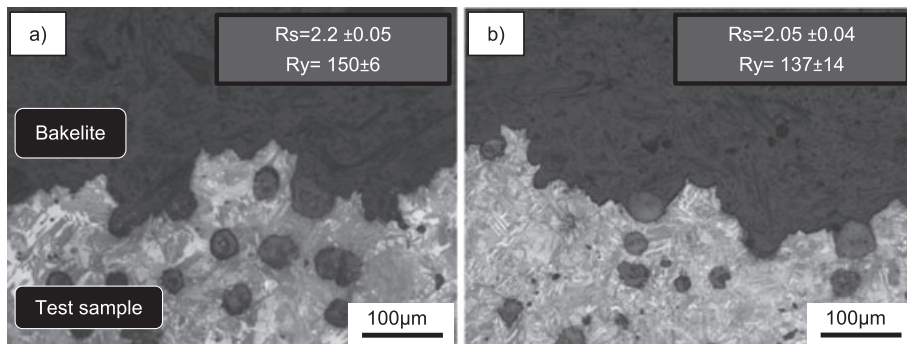

Fig. 9 Optical micrographs of the fracture profile resulting of bending test at room temperature (100×). a) ADI_{360}; b) ADI_{280}.

and frequencies.[10,26–32] In consequence, the authors believe that under cyclic loading conditions, the complex microstructure of ADI (graphite nodule, retained austenite, ausferrite and casting defects such as inclusions, microshrinkage pores, and irregularly shaped graphite clusters at or near the surface) leads to cleavage-like fracture mechanisms. This cleavage-like morphology evidenced in the fracture surface is recognized as a distinctive fracture mechanism that differentiates from the classic quasi-cleavage mechanisms observed for both quasi-static and dynamic loading conditions.

The fatigue crack path was also analysed by using optical metallography on a transverse section of the sample, in order to add information about the fracture surface morphology. This experimental methodology was also used by others authors.[10,29,32–35] The methodology

involves stopping the tests after several pre-established times before breaking the samples and then, obtaining the optical micrograph of the crack path as shown in Fig. 13. Secondary microcracks that emanate from the nodules (marked by white arrows) and the propagation of microcracks from the nodules towards the main crack (indicated by a black arrow) were observed in Fig. 13a. The crack path shows frequent small changes of direction, apparently indicating that the crack follows the orientation of ausferritic laths, which have a very small microstructural dimension (see Fig. 13b and c). A crack branching phenomena and secondary cracks that emanate from graphite particles are also observed (marked by white arrows). These observations are in concordance with the results reported by different authors. The ausferrite packet boundaries were assumed to act as
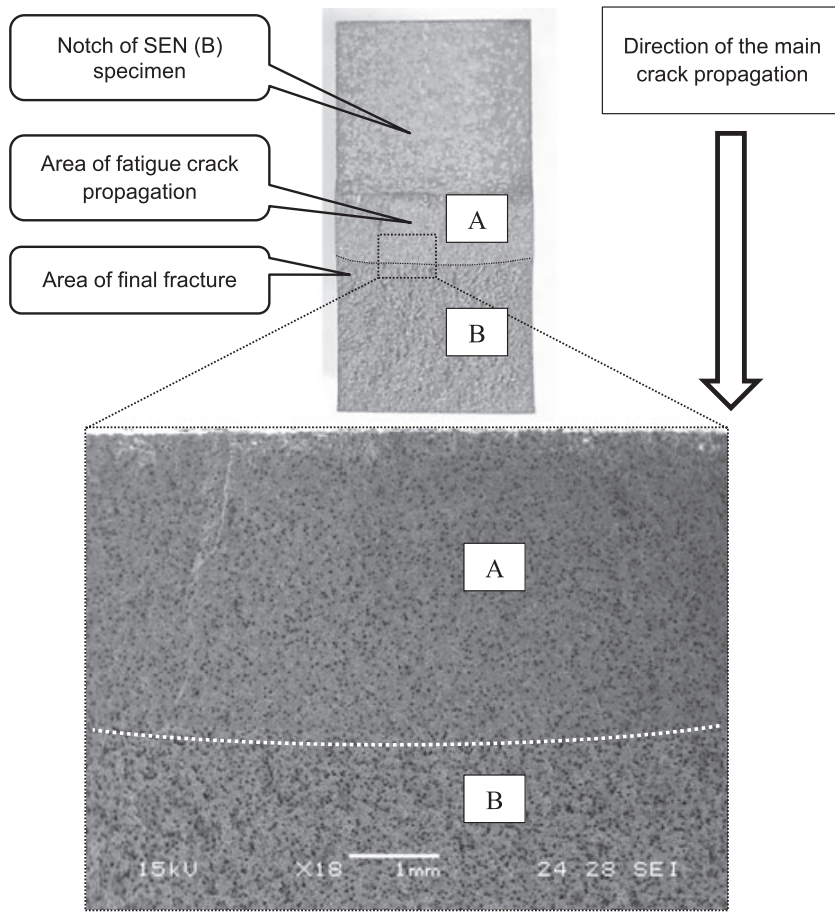
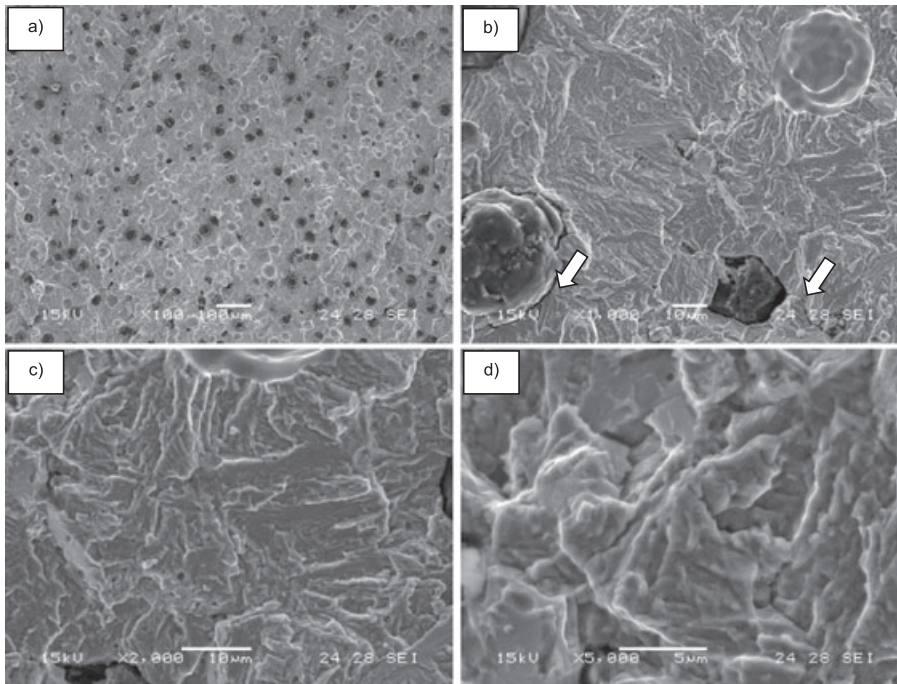**Fig. 10** Fracture surface resulting of fatigue test at macroscopic level.

Fig. 11 SEM image of the fracture surface resulting of fatigue tests at room temperature on ADI_{360}. Different magnifications.
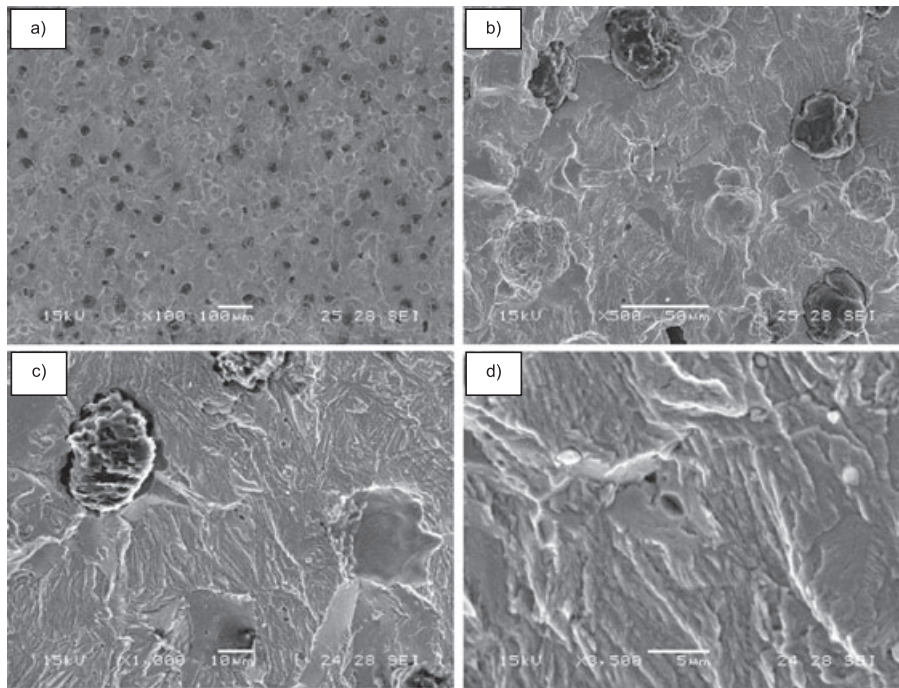
Fig. 12 SEM image of the fracture surface resulting of fatigue tests at room temperature on ADI$_{280}$. Different magnifications.
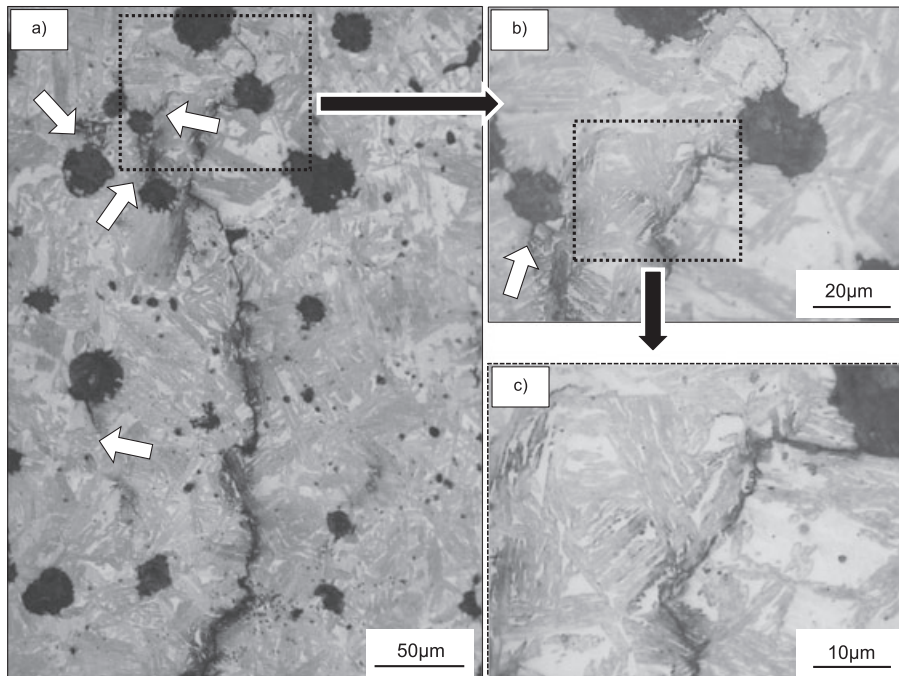

Fig. 13 Optical microscopy images. Main crack propagation under fatigue test on ADI.

barriers for microstructurally small cracks, and the strength of the barrier was proposed to depend on the relative orientations of the microstructure at the boundary.[36] In addition the fatigue crack was found to deflect following the orientation of ausferritic clusters,[34]

and also the initiation and growth of micro-cracks at the nodule cavity surface was proposed to lead to the deflection of the main crack.[35]

Figure 14 shows a detail of the crack propagation on ADI$_{360}$ at high magnification. A crack branching
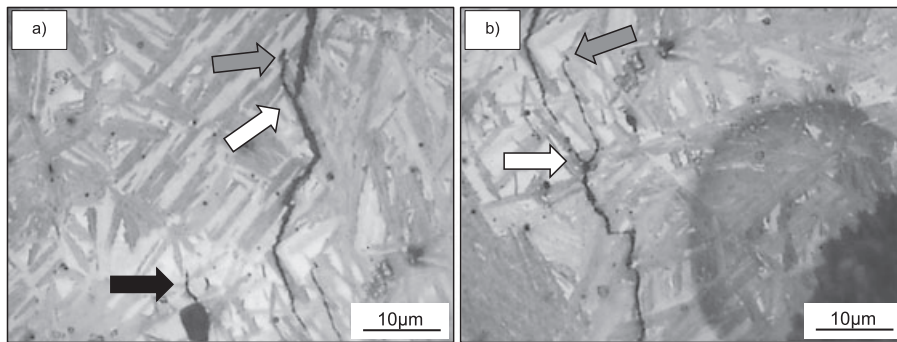
Fig. 14 Detail of the crack propagation at high magnification.

phenomena (marked by white arrows), crack propagation preferably through the ausferritic lath and a crack that emanates from the graphite nodule (marked by black arrow) are observed. The observation of crack arrest phenomenon in the retained austenite (marked by grey arrows in Fig. 14a and b) supports the hypothesis about the influence of the orientation of ausferritic laths in the fatigue crack propagation path and its influence on the fracture surface morphology.

An optical micrograph of the fracture profile is also shown in Fig. 15. The relatively flat appearance of the fracture profile topology, Fig. 15a, is in clear contrast with the relatively rough profile shown for both bending and impact tests (even at low temperatures). These differences are clearly reflected by the roughness measurements, which gave Rs and Ry values 30% and 60% respectively lower than those measured on bending tests, and 16% and 43% lower than those measured for impact test at $-20\,°C$ (compare Fig. 15 with Figs. 6 and 9). Meanwhile, cracks emanating from the nodule and joining to the main crack are also shown in Fig. 15b. Similar results were obtained for ADI_{280}.

In summary, the fatigue crack propagation by cyclic loads in ADI has shown four distinctive microscopic features: (1) the fatigue crack propagates by microcleavage; (2) there are no signs of striations; (3) both the nodular

contours and the matrix show negligible plastic deformation; and (4) the surface roughness is noticeably smaller than that characteristic of bending and impact fracture.

All these characteristics can be used to identify fatigue crack propagation in ADI as they differ from those typically found on impact and quasistatic fracture.

Main crack propagation direction and its relation with the topographic features
Fracture surfaces resulting of quasistatic and dynamic loading conditions

In recent publications, the authors have proposed methods to assess the crack propagation direction applicable to brittle and ductile fracture surfaces of ferritic and pearlitic DI.[12,13] In the present study, the results reported above for bending and impact tests showed fracture surfaces dominated by small quasi-cleavage facets and different levels of plastic deformation according to the test conditions. Accordingly, both methods would appear to be initially applicable to investigate the fracture propagation direction. However, in the case of ADI the very small quasi-cleavage facets do not show clear river patterns, and the methodology for brittle cleavage fracture cannot be applied. On the other hand, the enlargement of the nodular cavities by plastic deformation is noticeable, and therefore
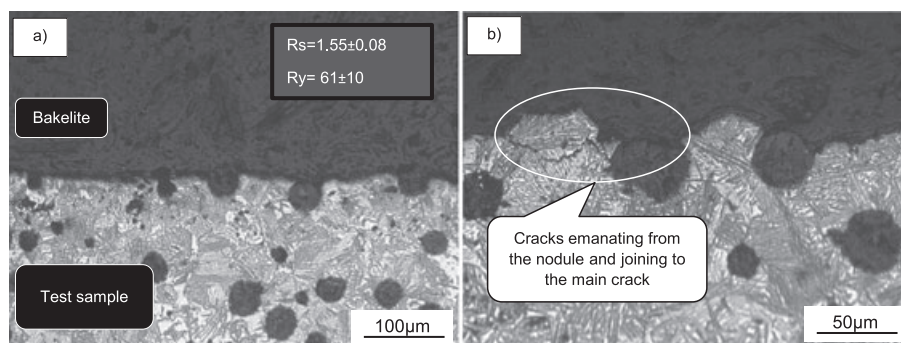

Fig. 15 Optical micrographs of the fracture profile resulting of fatigue test at room temperature at different magnifications on ADI_{360}. a) 100×; b) 50×.

the applicability of the 'ductile failure mode methodology' to investigate the fracture of ADI can be assessed. The method consists in identifying the crack propagation direction based on the measurement of the plastic deformation of the metallic matrix surrounding the graphite nodules. The characterization of the morphology of the cavities is carried out on digital images of the fracture surface observed under a graphic environment. The hypotheses of the methodology are that the determination of an equivalent ellipse in every nodular contour observed and the quantification of its deformation and orientation allow estimating the direction of the main crack propagation through the statistical analysis of a dataset. In all cases, the SEM fractographies were carefully obtained in order to maintain the same presetting orientation. Under these conditions, it is assumed that the direction of the main crack propagation is concordant with the notch plane. The samples were observed at the center of the fracture surface so that the edge effects are negligible. The methodology can be summarized as follows:

For each nodule present at the fracture surface, an ellipse is manually defined with the best possible fit to the deformed nodular contour. Then, the length of the nodular contour in axes parallel (Y) and perpendicular (X) to the main crack propagation direction, and the angle formed between the major axis of the ellipse and the main crack propagation direction (β) are measured. More details can be found in a recent paper by the authors.[12] A schematic representation of the parameters measured is shown in Fig. 16.

The results of measurements in both X-axis and Y-axis and a histogram of relative frequency for ADI_{360} are plotted in Fig. 17. Values of $Y/X = 1$ represent perfectly round nodular cavities. The plots show that most, but not all, nodule cavities deform along the main crack propagation direction. Similar results are obtained for ADI_{280}.

The results of the measurements of X, Y and the angle (β) on several fields of the samples studied are listed in Table 4. The results are grouped depending on the value of the Y/X ratio. The larger proportion of the contours of the nodular cavities show values of $Y/X > 1$ (Y axis predominant). The measurements of β angles show values at most of 9° with respect to the actual direction of the main crack propagation. Finally, considering that the reference Y-axis has been set along the main crack propagation direction, the low values of β prove that this method can be used to identify the direction of the main crack propagation with good approximation. The sense of propagation cannot be determined by this method. By evaluating the angle β, the results are independent from the reference axis chosen. Therefore, the procedure can be applied to identify the main crack propagation direction on a fracture surface, with good approximation. However, even though the results of the application of the method under the current experimental conditions are good, as in the case of ferritic DI, its effectiveness has to be yet evaluated under other testing conditions and geometries before it can be regarded as a general method.

Fracture surfaces resulting of cyclic loading conditions

For the particular case of fatigue fracture surfaces it was shown above that quasi-cleavage facets are dominant and little or no indication of ductile fracture mechanisms is found. Striations cannot be identified, nor used to assess fracture propagation direction. The small quasi-cleavage facts show little or no river patterns, preventing the use of the method applicable to brittle fracture. Finally, as the contour of the graphite nodule cavities show very little deformation, the ductile fracture method is not applicable either. As a result, no method to identify the fracture propagation direction in fatigue fractures of ADI on the basis of a microscopic analysis has been
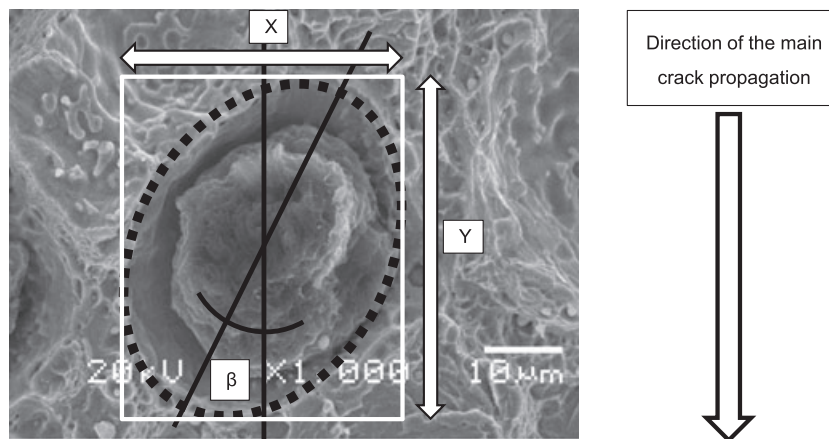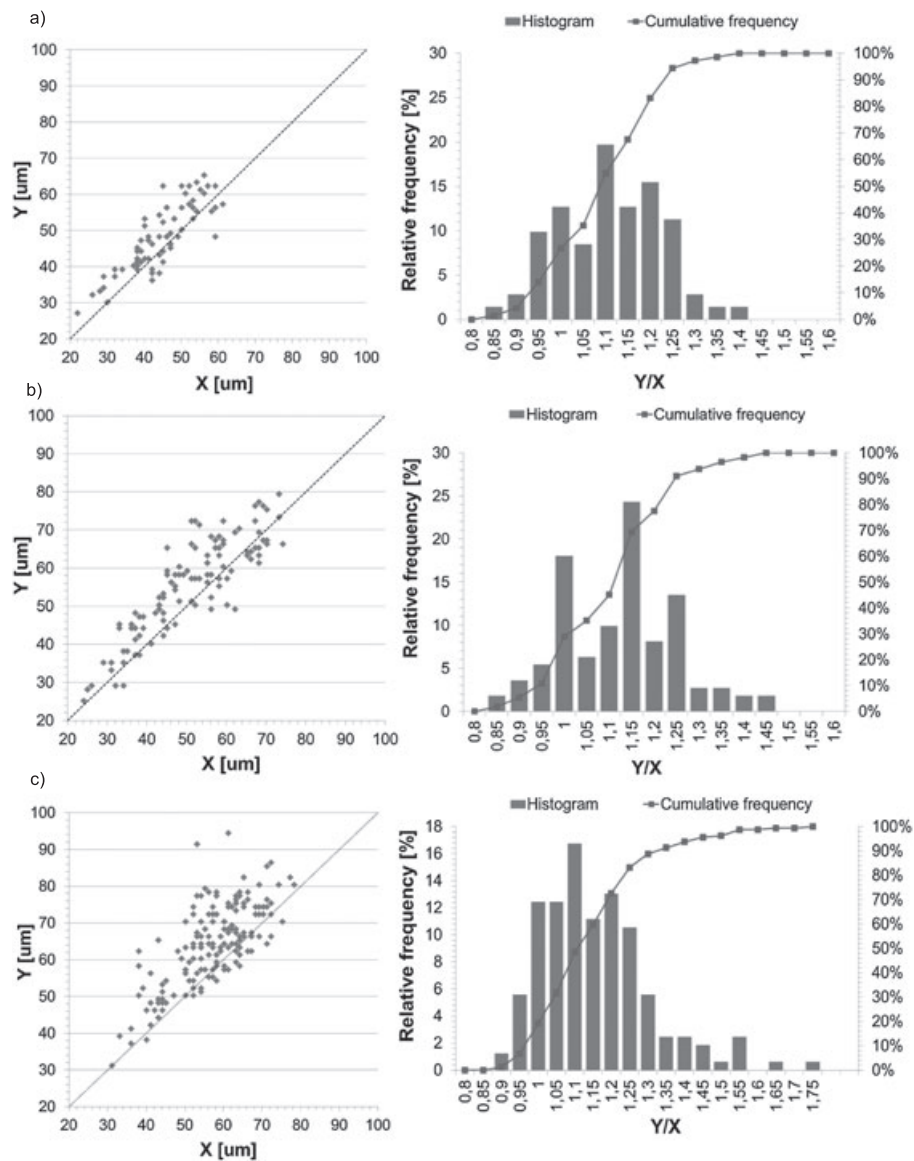

Fig. 16 Schematic representation of the parameters measured by using the ductile failure mode methodology.[12]

Fig. 17 Statistic plots from the experimental measurements of the X/Y ratio on ADI_{360}. a) Impact test at $-20\,°C$; b) impact test at $60\,°C$; c) bending test at room temperature.

Table 4 Results of methodology applied. Deformation of the contour of nodular cavities

Sample	Y-axis predominant [%]	Equiaxial [%]	Xaxis predominant [%]	Contours analysed	Angle of equivalent ellipse (β)
ADI360I-20	72	6	23	74	1.90 ± 0.28°
ADI360I60	68	7	24	111	2.20 ± 0.30°
ADI360Flx	78	11	12	161	9.00 ± 0.20
ADI280I-20	69	24	6	148	1.80 ± 0.2°
ADI280I60	72	22	5	139	0.70 ± 0.3°
ADI280Flx	77	7	16	135	4.40 ± 0.3

identified in this study. On the other hand, in this case fractographic features at macroscopic level allowed differentiating fatigue propagation regimes from final fracture as was shown in Fig. 10.

CONCLUSIONS

- Under impact loading, the predominant fracture mechanism changes from quasi-cleavage to ductile (with little

areas of cleavage facets) as the impact testing temperature increases. Noticeably, even at the lower temperatures tested, both ADI grades display some areas of ductile fracture and noticeable deformation of the nodular cavities.

- For bending test under quasi-static loading conditions at room temperature, a mix of cleavage facets, deformation of contours of nodular cavities and microvoid coalescence characterize the fracture surface of ADI, as in the case of impact fracture.

- The fatigue crack propagation by cyclic loads in ADI has shown four distinctive microscopic features: (1) the fatigue crack propagates by microcleavage; (2) there are no signs of striations; (3) both the nodular contours and the matrix show negligible plastic deformation; and (4) the surface roughness is noticeably smaller than that characteristic of bending and impact fracture. All these characteristics can be used to identify fatigue crack propagation in ADI as they differ from those typically found on impact and quasi static load fracture.

- The applicability of a methodology for the determination of the main crack propagation direction on fractured ADI proposed by authors in a recent paper was assessed. For bending and impact fractures the methodology was effective, allowing the determination of the direction of propagation of the main crack with good accuracy. This was possible because graphite nodule cavities suffer noticeable deformation during fracture, even under impact loading at low temperature. On the other hand, for fatigue fracture, no fractographic features were useful to identify the direction of propagation of the crack.

Although the conclusions reported above are based on solid experimental evidences, the authors believe that it is necessary to extend the analysis to other experimental conditions, such as samples with different nodular count, mixed loading conditions, geometry and size, before these results can be judged of general validity.

Acknowledgements

REFERENCES

1 Burditt, F. M. (1992) *Ductile Iron Handbook*, American Foundrymen's Society, Inc.: Des Plaines, Illinois, USA, pp. 31–36.

2 Kovacs, B. V. (1987) Development of austempered ductile iron (ADI) for automobile Crankshafts. *J. Heat Treat.*, **5**, 55–60.

3 Davis, R. J. (1990) *Metals Handbook, Vol. 11*, 9th ed, Failure Analysis and Prevention. American Society for Metals: Ohio, USA.

4 Fellows, A. J. (1973) *Metals Handbook, Vol. 9*, 8th ed, Fractography and Atlas of Fractographs. American Society for Metals: Ohio, USA.

5 Villacis Verdesoto, W. and Sikora, J. A. (1989) Crack initiation and propagation in spheroidal graphite cast iron with different micromorphologies. *Cast Metals*, **1**, 210–215.

6 Voigt, R. C. and Eldoky, L. M. (1986) Crack initiation and propagation in as-cast and fully pearlitic ductile cast irons. *AFS Trans. Minneapolis, Minnesota, USA*, **86**, 637–644.

7 Hafiz, M. F., Hammouda, A. and El-Gemae, S. (2005) Impact properties and fractography of spheroidal graphite cast irons. *AFS Trans., Schaumburg, II USA*, **5**, 2–12.

8 Davis, J. (1996) Cast irons/metallurgy and properties of ductile cast irons. In: *ASM Specialty Handbook*, The Materials Information Society: USA.

9 Rajnovic, D., Eric, O. and Sidjanin, L. (2008) Transition temperature and fracture mode of as-cast and austempered ductile iron. *J. Microsc.*, **232**, 605–610.

10 Martínez, R. A. (2010) Fracture surfaces and the associated failure mechanisms in ductile iron with different matrices and load bearing. *Eng. Fract. Mech.*, **77**, 2749–2762.

11 Kokavec, M., Konečná, R. and Nicoletto, G. (2011) Influence of surface quality on fatigue behavior of nodular cast iron. *Acta Metallurgica Slovaca*, **17**, 99–105.

12 Fernandino, D. O. and Boeri, R. (2015) Study of the fracture of ferritic ductile cast iron under different loading conditions. *Fatigue Fract. Eng. Mater. Struct.*, **38**, 610–620.

13 Fernandino, D. O. and Boeri, R. (2015) Fracture of pearlitic ductile cast iron under different loading conditions. *Fatigue Fract. Eng. Mater. Struct.*, **38**, 80–90.

14 Tada, H., Paris, P. C. and Irwin, G. (2000) *The Stress Analysis of Cracks Handbook*, 3rd ed, ASME press: New York. Part II, pp. 58–59.

15 Underwood, E. and Banerji, K. (1987) *Metals Handbook*, 9th ed, Vol. **12**, ASM: Metals Park, pp. 193–211.

16 Fierro, V. E., Sikora, J. A., Agüera, F. R., Alvarez Villar, H. N., Ansaldi, A. F. and Ratto, P. J. J. (2000) Comportamiento mecánico de fundiciones esferoidales entre −100 °C y 200 °C. In: *Congreso binacional de metalurgia y materiales SAM/CONAMET—IV Coloquio Latinoamericano de Fractura y Fatiga*, Neuquén: Argentina, pp. 93–100.

17 Ipohorski, M. and Acuña, R. J. (1988) *Fractografía. Aplicación al Análisis de Fallas*, Buenos Aires: Comisión Nacional de Energía Atómica.

18 Fan, Z. K. and Smallman, R. E. (1994) Some observation on the fracture of austempered ductile iron. *Scripta Metallurgica Materialia*, **31**, 137–142.

19 Dai, P. Q., He, Z. R., Zheng, C. M. and Mao, Z. Y. (2001) In-situ SEM observation on the fractured austempered ductile iron. *Mater. Sci. Eng. A*, **319–321**, 531–534.

20 Kilicli, V. and Erdogan, M. (2010) The nature of the tensile fracture in austempered ductile iron with dual matrix microstructure. *J. Mater. Eng. Perform.*, **19**, 142–149.

21 Ritchie, R. O. (1997) Near-threshold fatigue crack propagation in ultra-high strength steel: influence of load ratio and cyclic strength. *J. Eng. Mater. Technology*, **99**, 195–204.

22 Ritchie, R. O. (1999) Mechanisms of fatigue-crack propagation in ductile and brittle solids. *Int. J. Fracture*, **100**, 55–83.

23 Suresh, S. (1991) *Fatigue of Materials*, Cambridge University Press: Cambridge.

24 Helzberg, R. W. (1996) *Deformation and Fracture Mechanics of Engineering Materials*, 4th ed, John Wiley & Sons, Inc., New Jersey, USA.

25 Stephens, R. I., Fatemi, A., Stephens, R. R. and Fuchs, O. H. (2001) *Metal Fatigue in Engineering*, 2nd ed, John Wiley & Sons, Inc., New York, USA.

26 Lin, C. K., Lai, P.-K. and Shih, T.-S. (1996) Influence of microstructure on the fatigue properties of austempered ductile irons. High-cycle fatigue. *Int. J. Fatigue*, **18**, 297–307.

27 Lin, C. K. and Hung, T. P. (1996) Influence of microstructure on the fatigue properties of austempered ductile irons. Low-cycle fatigue. *Int. J. Fatigue*, **18**, 309–320.

28 Tayanc, M., Aztekin, K. and Bayram, A. (2007) The effect of matrix structure on the fatigue behavior of austempered ductile iron. *Mater. Design*, **28**, 797–803.

29 Cavallini, M., Di Bartolomeo, O. and Iacoviello, F. (2008) Fatigue crack propagation damaging micromechanisms in ductile cast irons. *Eng. Fract. Mech.*, **75**, 694–704.

30 Elsayed, A. H., Megahed, M. M., Sadek, A. A. and Abouelela, K. M. (2009) Fracture toughness characterization of austempered ductile iron produced using both conventional and two-step austempering processes. *Mater. Design*, **30**, 1866–1877.

31 Zhang, J., Song, Q., Zhang, N., Lu, N., Zhang, M. and Cui, G. (2015) Very high cycle fatigue property of high-strength austempered ductile iron at conventional and ultrasonic frequency loading. *Int. J. Fatigue*, **70**, 235–240.

32 Greno, G. L., Otegui, J. L. and Boeri, R. E. (1999) Mechanisms of fatigue crack growth in austempered ductile iron. *Int. J. Fatigue*, **21**, 35–43.

33 Basso, A., Martinez, R., Cisilino, A. and Sikora, J. (2009) Experimental and numerical assessment of fracture toughness of dual-phase austempered ductile iron. *Fatigue Fract. Eng. Mater. Struct.*, **33**, 1–11.

34 Bubenko, L., Konečná, R. and Nicoletto, G. (2009) Observation of fatigue crack paths in nodular cast iron and ADI microstructures. *Mater Eng.*, **16**, 13–18.

35 Stokes, B., Gao, N. and Reed, P. A. S. (2007) Effects of graphite nodules on crack growth behavior of austempered ductile iron. *Mater. Sci. Eng. A*, **445–446**, 374–385.

36 Chapetti, M. D. (2007) High-cycle fatigue of austempered ductile iron (ADI). *Int. J. Fatigue*, **29**, 860–868.